Aerospace Science and Technology 161 (2025) 110103

Contents lists available at ScienceDirect

Aerospace Science and Technology

journal homepage: www.elsevier.com/locate/aescte

Modeling impact of drones on flat plates

Jay McNeill [a], Randall VanDyk [a], C.H.M. Simha [a,*], Azzedine Dadouche [b], David Backman [b], Manouchehr Nejad Ensan [b], Javad Gholipour [c]

[a] School of Engineering, University of Guelph, 50, Stone Road East, Guelph, ON N1G 2W1, Canada
[b] National Research Council, 1200 Montreal Rd. Ottawa, Ontario K1A 0R6, Canada
[c] National Research Council, 2107, ch. Polytechnique, Campus de l'Université de Montréal, Montréal, Québec, H3T 2B2, Canada

ARTICLE INFO

Communicated by Marwan Al-Haik

Keywords:
Drone impact
Finite element modeling
Simplified modeling

ABSTRACT

Experiments on the impact of cannon-launched Phantom DJI 3 quadcopters onto 1-m square aircraft-grade aluminum flat plates (1.6 mm and 6.35 mm thick) at velocities of 130 m/s (250 knots) and 70 m/s (140 knots) are presented, and finite element modeling of the impacts is also described. Load histories at the corners of the plate, central deflection, and possible perforation of the plate are modeled and compared with experimental results. Failure of drone components was modeled, as they were significantly damaged in all of the tests. Failure of the plate was also modeled, as in the high-speed tests with thin plates, the drone perforated the plate. Predictions of the total peak load on the plates are within 20% of the experimental values and the central deflections are within 10% of the experimental values. Additionally, modal analysis reveals that the characteristic half period of 5-6 ms observed in the load histories corresponds to the natural frequencies of the structure that holds the plate in the test. Using the insights gained from the simulations, simple analytical models, wherein the components of the drone are modeled as blunt, rigid objects and the target is modeled as mass and dashpot, were developed. These yield second-order ordinary differential equations whose solutions provide rapid estimates of the peak load and deflection in all tests to within 15% of the experimental values. To estimate the threshold impact velocity to perforate the plate, an analytical model is presented. The major contributions of this article are validated work flows to develop drone finite element models that do not require extensive characterization of drone components, and simplified analytical models for rapid assessment of drone impacts.

1. Introduction

Unmanned Aerial Vehicles (UAVs) may pose a threat to the safety of passenger aircraft. For instance, the DJI Phantom 3, the drone studied in this work, can reach an altitude of 6000 m (19,800 ft). The flight speed of an aircraft at this height is approximately 194 km/h (380 knots) and collision with a drone may cause significant damage.

Accordingly, the need for government regulations and aircraft design certification procedures has spurred several governmental regulators to sponsor studies of drone impacts based on: theoretical methods to assess impact damage; impact experiments using gas guns; and experimental studies in combination with finite element computation. Experimental studies have included impacts of drones on different parts of the aircraft such as the windshield, canopy, or the leading edges of horizontal stabilizers and wings. The first theoretical study was carried out by Monash University and the Civil Aviation Authority in Australia to estimate the minimum impact velocity of a drone that causes critical damage to an aircraft; Radi [1].

The Military Aviation Authority (MAA), British Airline Pilots Association (BALPA), and the Department for Transportation in the United Kingdom commissioned the first experimental study on "Small Remotely Piloted Aircraft Systems" that examined the effects of a mid-air collision between drones and aircraft [2].

Under the aegis of the United States' Federal Aviation Authority, The National Institute for Aviation Research (NIAR) at Wichita State University, launched a comprehensive experimental and computational modeling program of study to assess the effects of the interaction of an aircraft with a quadcopter. Olivares et al. [3] present a comprehensive overview of the program; and Olivares et al. [4] detail the effects of quadcopter impact onto commercial transport and business jets. They

* Corresponding author.
E-mail addresses: csimha@uoguelph.ca (C.H.M. Simha), azzedine.dadouche@nrc-cnrc.gc.ca (A. Dadouche).

https://doi.org/10.1016/j.ast.2025.110103
Received 21 October 2024; Received in revised form 19 February 2025; Accepted 25 February 2025
Available online 27 February 2025

used an explicit dynamics finite element solver to model the impact of a DJI Phantom 3 drone onto an aircraft and also compared effects of the impact with damage caused by equivalent birds. Their drone modeling is underpinned by detailed testing and modeling efforts for each of the *drone components*.

Force-displacement measurements from static and drop-tower tests on drone components (not the drone assembly) were used to develop and validate finite element models of the components. Computational predictions of the force-displacement curves were found to be in excellent agreement with the measurements. Each of the *components* were launched at 51.4 m/s (100 knots) and 128.6 m/s (250 knots) against flat plates of 2024-T3 aluminum (1.6- to 6.34-mm thick) using a gas gun, and the loads at the corners of the plate and strains in the center were measured. Impact simulations using the LS-DYNA explicit solver were carried out and agreement with experimentally measured histories were within 10%. For thick target plates, the component did not penetrate the plate. With the validated models of the drone components in hand, Olivares et al. [4], performed drone assembly impact simulations onto commercial transport jet and business jet aircraft with impact locations varying from windshield to the horizontal and vertical leading edge. The results show that the damage to the commercial transport jet and the business jet at 250 knots (128 m/s) is medium to high for the horizontal and vertical stabilizers, medium damage to the leading edge of the wing, and medium to low damage for the windshield.

The Nanjing University, Northwestern Polytechnical University and the Shanghai Aircraft Airworthiness Certification Center collaborated to conduct a study of airborne collision between drone (DJI Phantom quadcopter) and an aircraft nose Lu et al. [5]. The PAM-CRASH software was used to perform Finite Element (FE) simulations.

Another combined experimental-computational study was conducted by the Nanjing University, Northwestern Polytechnical University and the Shanghai Aircraft Airworthiness Certification Center in China Lu et al. [6]. They studied airborne collisions between drones and an aircraft windshield. Four drone models (Spark, Mavic, Phantom 4 Pro, and Inspire) of varying masses were impacted onto different locations of an aircraft windshield.

Meng et al. [7] at the Nanjing University, Northwestern Polytechnical University and the Shanghai Aircraft Airworthiness Certification Center studied the airborne collision between a drone (Inspire I quadcopter) and a horizontal stabilizer of an aircraft. They performed one experiment and simulated four tests on four different locations on the stabilizer at three different speeds (120 151 and 180 m/s).

It is useful to gather some observations from the experimental and modeling effort reported in the literature.

1. Impact tests have shown that owing to higher densities and stiffness of drone components, drone strikes led to more severe damage than impact with birds. Current designs certified for birdstrike would not be suitable against drone impacts as the drones have greater kinetic energy loss when compared to birds. This implies that the drone strike has a higher peak load (than bird strikes) and causes more serious damage because of the strength of its major components.
2. The highest-mass drone components such as battery, camera, and motors cause the most significant damage during impacts. Mass of the individual components and their configurations affects the impact loads and deformation of the plate.
3. Modeling drone impact involves complex workflows. Specifically, drone components are scanned to obtain a cloud of points, which is then converted into a solid model. This solid model can be meshed and assigned boundary conditions, initial conditions, and material properties, and a finite element model created for input to an explicit time integration, non-linear dynamics code.
4. Extensive component-level testing with ballistic *impact onto plates* has been very successful; agreement between finite element models and simulations is excellent; Olivares et al. [4]. It bears emphasis that such models are not openly available, and development of models for newer designs and configurations of drones demands repetition of the effort.
5. Impact of drone assembly model onto *aircraft structures* has met with some success; the agreement between finite element model predictions and experimental histories are reasonable from an engineering stand point; however, the agreement is not as good when compared to the component-level testing.

As it stands, workflows to develop drone models for impact onto targets and aircrafts exist, and the predictions of these models are acceptable for engineering purposes; here, it is assumed that any computational prediction that is within 10% of the experimental value is deemed acceptable. The workflows include a sequence of softwares: to convert scanned component models into solid models, to assemble the solid models and mesh them; to obtain the solver file; and to carry out the finite element computations. However, it bears emphasis that the workflows are complex and involves multiple softwares, significant expertise, and, based on our experience, substantial time investments. Also, the drone impact computations are computationally expensive. Note that owing to availability of many drone models, with varying configurations and component masses, the latter workflow has to be repeated to develop models.

Furthermore, there are no reports of the modeling of drone impact onto instrumented flat plates. The foregoing motivates the following questions:

1. **Without carrying out detailed component-level testing,** can we develop a finite element model of the impact of a drone onto a flat aircraft-grade aluminum plate? Specifically, predict the following: load histories on the perimeter of the plate, strains in the plate, and whether the plate is perforated/not perforated for the given orientation and impact velocity of the drone.
2. **Based on the results of the finite element modeling, can we develop simplified models (at the level of ordinary differential equations) for rapid assessments of effects of drone impacts onto plates? Specifically, predict whether penetration will occur, estimate peak loads, typical features of the load histories, and deflections.** Given the variety of drone models (with varying masses and configurations), this is a crucial question because of the involved workflows described above are unsuitable for rapid assessments.

This work presents results of impact tests of quadcopters onto flat plates of varying thickness with attendant measurements of load histories and plate deformation. Experiments were carried out at the impact test facility of the National Research Council (NRC) of Canada; Dadouche et al. [8]. Without carrying out component-level testing, finite element model of the drone-assembly was developed and used to model the tests. Results of the computational models inform the development of simplified models. It is important to emphasize that the experiments and models in this work are limited to the impacts of drones on plates wherein the motors lead the impact event. More severe yaw, pitch, and roll orientations, are not considered. Impacts onto aircraft structures, notably the Horizontal Stabilizer, will be addressed in a sequel.

This paper is organized as follows. In Section 2, the experiments carried out at NRC are described, Sections 3 and 4 details finite element modeling and validation efforts, and Sections 5 and 6 describes development of simplified models of drone impact and penetration, respectively. Finally, the article concludes with a summary and future directions.

2. Experimental details

Details of the experimental testing facility and impact tests may be found in the report by Dadouche et al. [9]; a brief description is given here. Fig. 1 shows images of the test facility, target mount, and speckle

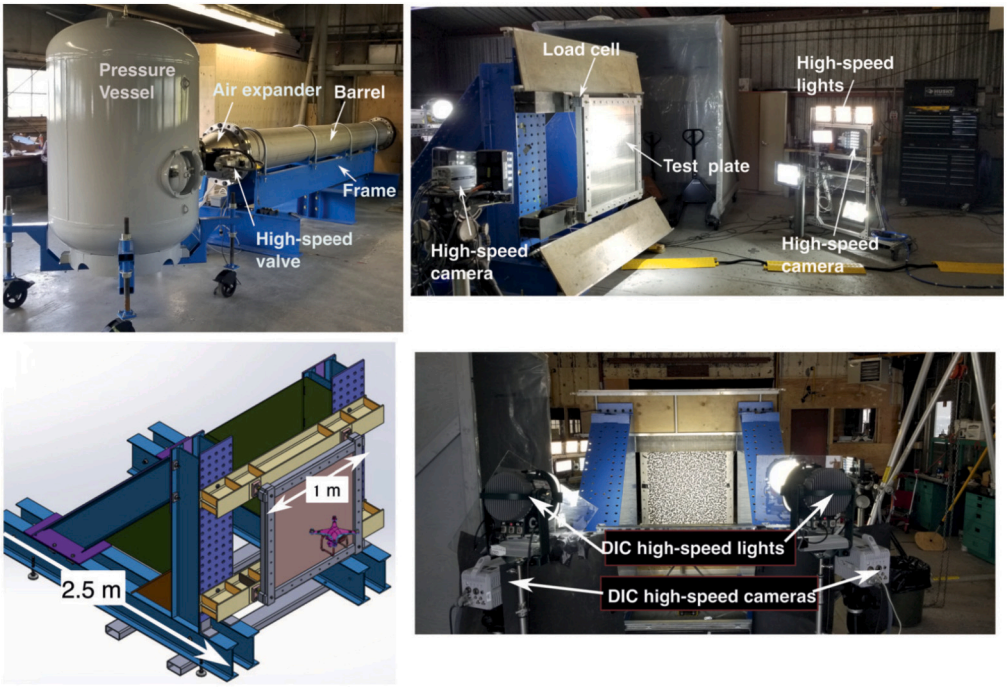

Fig. 1. Experimental set up: a) 17.25-in. diameter drone cannon, b) Overall test set-up, c) Solid model of structure with target plate and drone d) Set-up of digital image correlation system.

Table 1
Velocity and orientation measured with high-speed cameras.

Test #	Thickness. [mm]	Velocity [m/s]	Roll [^{o}]	Pitch [^{o}]	Yaw [^{o}]	Notes
1	1.6	129.38	12.7	10.2	6.7	Penetration
2	1.6	129.54	11	3.8	6.8	Penetration
3	1.6	69.19	8	0	43	Tearing with no penetration
4	1.6	70.56	40-42	2	37-40	Severe damage
5	1.6	71.32	85	8.8	17.3	Severe damage
6	6.35	130.46	13.2	4.5	7.5	Dents, no penetration
7	6.35	128.92	13	3.5	2.3	Dents, no penetration*
8	6.35	71.30	4.5	2	9	Minor dents
9	6.35	72.13	40	8.2	11.4	Minor dents

* Test 7 had a fully charged battery and there was significant smoke from the drone after impact.

pattern on target for Digital Image Correlation (DIC). The 17.25-in. diameter cannon is connected to a pressure vessel through an air expander and a fast-release valve. The pressure vessel has a capacity of 1.7 m^3 (450 gallons) and certified up to 1 MPa (150 psi). In the present work, DJI Phantom 3 Quadcopter (1.13 kg nominal weight) was launched using split foam sabots; Dadouche et al. [9]. The barrel plus extender are approximately 6.6 m long, and there is approximately 4.4 m of free flight before the drone impacts the target. Impact velocity and orientation (roll, pitch and yaw) were measured using high-speed cameras at a standoff distance of 300 mm from the target. Targets were 1.6-mm and 6.35-mm thick 2024-T3 aluminum plates. Additional high-speed cameras were used to capture video of the deforming speckle pattern, which was analyzed using DIC to obtain strains.

Impact velocities of 72 m/s (140 knots) and 128 m/s (256 knots) were used as the former corresponds to speed at 30468 m (10,000 ft), and the latter to approach landing speed. To achieve a velocity of 72 m/s a nominal pressure of 117 kPa (17 psi) was used, and to achieve a velocity of 128 m/s the nominal pressure was 275.8 kPa (40 psi).

Table 1 summarizes details of the testing; when fully charged batteries were used in the test, they posed a fire hazard with open flames from the damaged batteries were observed immediately after the impact event.

Fig. 2 presents post-test photos of the target. In Test 1, and 2 there was significant, tearing, petaling and complete penetration by the drone. The perimeter of the torn area corresponds approximately with the bounding perimeter of the impacting drone. In Test 3 (1.6 mm, 69 m/s), there was some tearing with no full penetration. Hereafter, two numbers in parentheses, after a test number, denote plate thickness and drone impact velocity in m/s.

In Test 4 and Test 5 (not shown here) there was severe damage with no tearing. For low velocity (71 m/s) impacts onto thick and thin plates, the target showed minor dents, but no penetration.

Load histories recorded in some of the tests are shown in Fig. 3. In Test 1 (1.6, 129) and Test 4 (1.6, 70) the plate thickness was the same, but in the former there was full penetration. Peak load also depends on the orientation of the drone at the time of impact. When the plate thickness or impact velocity is increased, the peak load increases. Note that the signals appear to have a half-period of 5 ms. The graph at the bottom of the figure highlights an important aspect of the signals. Here the load histories from the four cells in Test 1 (1.6, 129) and Test 9 (6.35, 72) are summed and plotted. We superpose a half-sine wave with

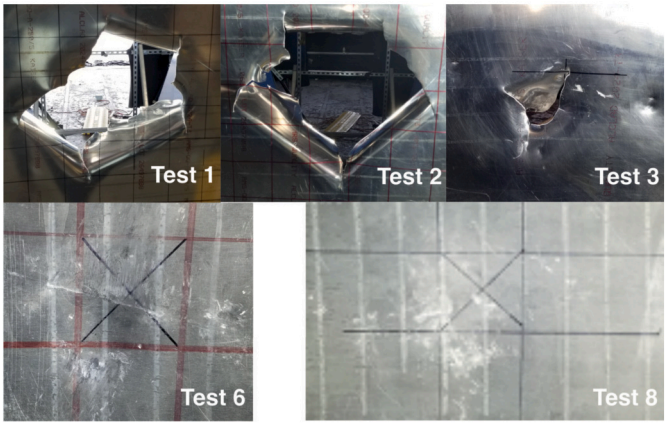

Fig. 2. Post-test photographs of the plate. Plates in Test 1 (1.6 mm, 129 m/s) and 2 (1.6, 129) showed full penetration - note the significant tearing and petaling. Plate in Test 3 (1.6, 69) had partial penetration. Plates in Test 6 (6.35, 130) and Test 8 (6.35, 71) showed dents caused by the motors and the battery.

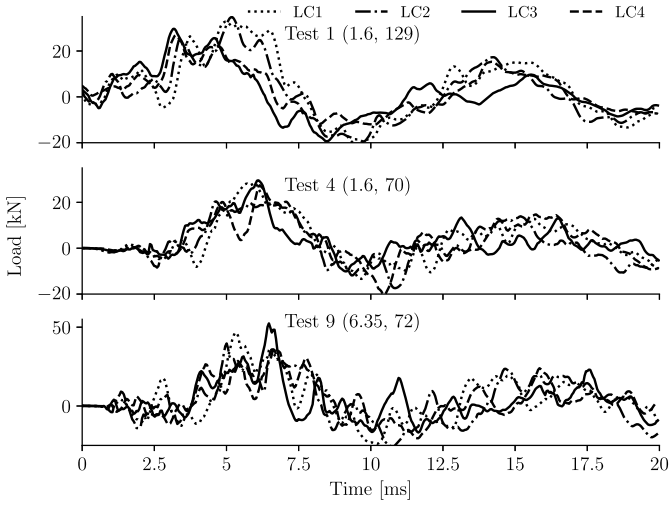

Fig. 3. Load histories on the plate measured by the load cells. Peak load is dependent on thickness and impact velocity. All of the signals display an approximate half-period of 5 ms.

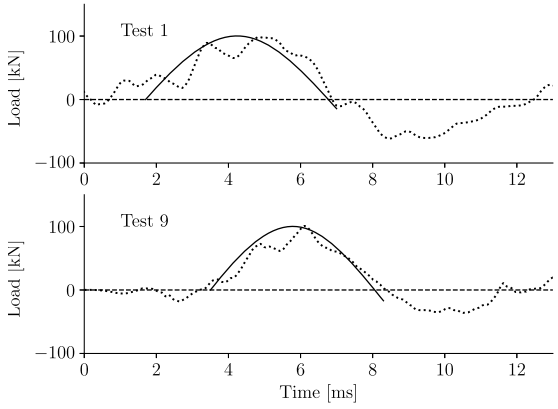

Fig. 4. Summed load histories on the plate measured by the load cells. Peak load is dependent on thickness and impact velocity. Half-sine wave with half-period of 5 ms well approximates the first part of the signal.

a half-period of approximately 5 ms to emphasize that the initial part of the signal can be approximated (see Fig. 4).

3. Finite element model

The work-flow to obtain the finite element model included three different softwares: Geomagic to convert the scanned components to solid models, SolidWorks to assemble the components and develop target models, Hypermesh the pre-processor to obtain the keyword files that serve as input to the explicit time integration, non-linear dynamics finite element solver LS-DYNA.

3.1. Drone components - solid model, mesh, and contact

The drone components were scanned using an ATOS Core 3D laser scanner system from GOM (currently Zeiss) and a cloud of points in the form of a STereoLithography (STL) file was obtained. Owing to the resolution of the scanner, all of the features in the components are captured in the cloud of points. For instance, see image of bottom casing in Fig. 5.

The software program Geomagic, was used to convert the cloud of points obtained using laser scans to 3D solid models. It is reasonable to assume that many of the smallest features and finer details do not play a role in the impact response of the drone and furthermore, whilst meshing these features will result in a very fine mesh around the holes and features. The latter leads to significant computational times owing to the dependence of the time step on the element size and sound speed. Accordingly, those features, deemed to not contribute to the impact response are removed or smoothed out. See for instance, the de-featured bottom cover in Fig. 5. Components that are thin-walled (of the order of a few mm) were converted to surfaces, and bulk bodies were converted to solids. Fig. 6 shows some of the drone components; camera, battery and motors are treated as solids and meshed with tetrahedral elements; and landing gear is treated as a surface and meshed with four-noded shell elements.

All of the resultant solid and surface models were imported into SolidWorks to ensure that all of the components fit together when assembled. For instance, the top casing was adjusted in SolidWorks to properly align it with the bottom casing and therefore allowing for surface to surface contact. The bottom cover was also adjusted in SolidWorks to create a slot for the battery to fit into, and the landing gear was adjusted to improve planarity of the surfaces. Finally, the frame structure that contained the plate was also created in SolidWorks. After these adjustments were made, they were exported as Standard for the Exchange of Product Data (STEP) files that could be imported into the Hypermesh pre-processor.

Hypermesh was used to mesh the solid models of the drone, target, set boundary conditions, assign initial translation and rotational velocities of the drone, assign component material properties, and output the input file for the finite element solver. Each component was assigned material properties such as density, elastic modulus and yield stress and the shells were assigned section properties such as thickness. The density of the drone casing material and some of the other components was slightly altered to compensate for the electrical wiring and other components on the inside that were not modeled. That is, the densities were adjusted so that the mass in the model was equal to the measured mass of the component. This is particularly crucial in case of the motors of the quadcopter which, as will be seen later, are crucial to the modeling of penetration as it first interacts with the target. The total mass of the drone was equal to the mass of the drone used in the experiments. Drones were given the same orientation (roll, pitch, and yaw) as in the experiment.

There were two types of elements that were used in meshing the drone - shell and solid elements. Tetrahedral elements were used to mesh 3D objects, shell elements were assigned to the 2D objects and given a thickness through its properties. All components were given an initial mesh size and convergence, especially in the force results, was verified by refining the mesh size. The flat plate, landing gear and drone casing were the components meshed with shell elements and all of the latter components were modeled as 2D surfaces. Finer mesh leads to

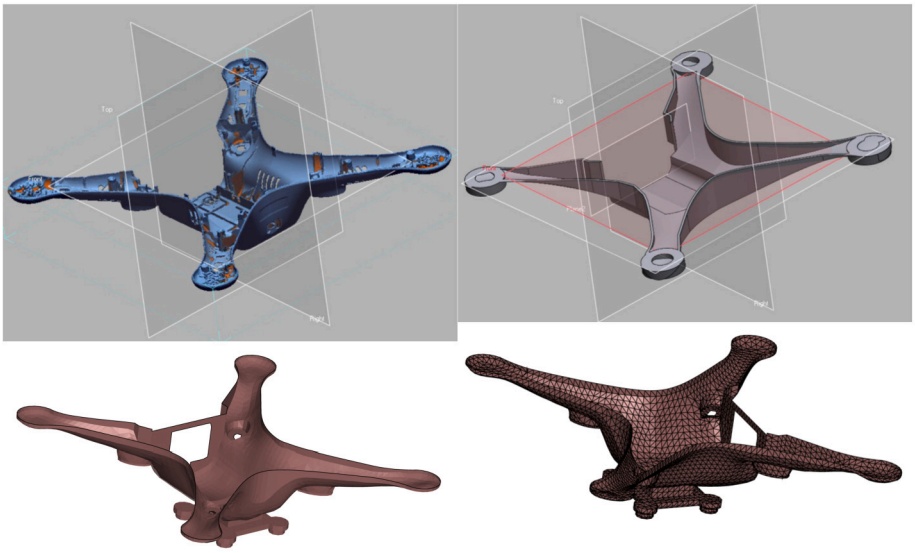

Fig. 5. Top left: cloud of points from scanned bottom casing viewed in Geomagic. Top right: de-featured casing. Bottom left: shell version of bottom casing. Bottom right: bottom casing meshed with shell elements.

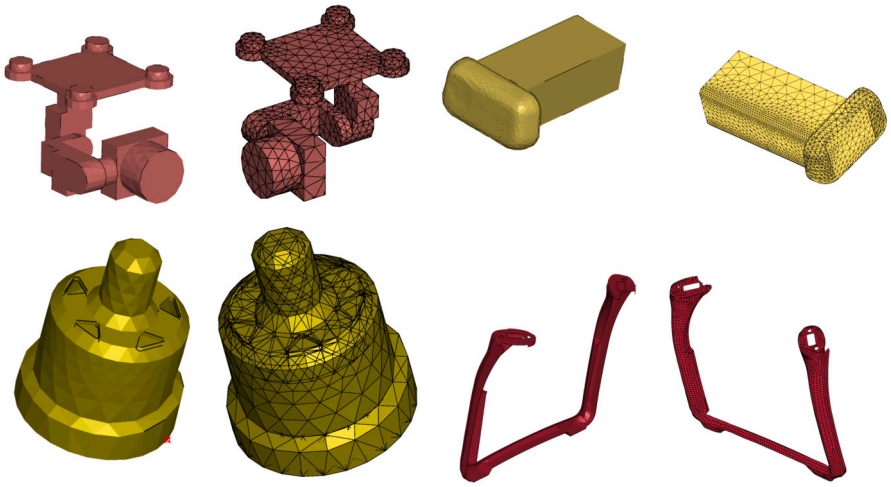

Fig. 6. Top left: solid model of camera and meshed part. Top right: solid model of battery and meshed part. Bottom left: solid model of motor and meshed part. Bottom right: surface model of landing gear and meshed part.

smaller time steps and coarser mesh may yield mesh-dependent results. Based on trial-and-error, the mesh size was optimized. Coarser mesh, for certain parts of the model, were used so that computational time would be reduced. The curvature and cleanup elements tools were used in this case to optimize and smoothen the mesh to allow for a coarser mesh in locations where a fine mesh was not needed. The complete drone model and flat plate assembly consisted of 442,629 elements and 153,552 nodes. Mesh quality assessments and Jacobian plots for the mesh may be found in the thesis by McNeill [10]. Table 2 summarizes element and mesh details.

Contact surfaces and node sets were created for contact algorithms and assignment of points for connection of the pieces of the drone. Constrained tie break contact algorithm was used to connect nodes with other nodes, used to connect the drone body top and bottom together, and a strain value (0.1) assigned for separation; strain was calibrated by a trial-and-error process; and comparison of the simulation results with the high-speed video. Contact tiebreak surface to surface is used when connecting two contact surfaces together and a stress value is used to determine the point of separation. A contact algorithm was assumed between all nodes of the drone and the contact surface of the flat plate to allow them to collide, slide and penetrate. Load cells were added to the four corners of the flat plate to record the force of impact in a manner similar to the experiments. It bears emphasis that for the battery, the soft contact algorithm was used because it was modeled as a foam as described later.

Table 2
Mesh and element details.

Component	Element Type	Size(s) [mm]	Notes
Battery Motor Camera	4-noded Tetrahedron	4	ELFORM 1
Landing Gear Casing	5-layer Shell	2.5 6	ELFORM 2 ELFORM 16
Target Plate	5-layer shell	2, 10	ELFORM 16
I Beams Load Cells	4-noded Tetrahedron	4 4	ELFORM 1 ELFORM 1

ELFORM 1 is a four-noded tetrahedron with reduced integration.
ELFORM 16 was used for better modeling failure.
ELFORM 2 is the standard Belytschko-Tsay shell element.
Target plate had a fine mesh in the center and a coarse mesh on the outside.

Table 3
Drone component material parameters.

Parameter	Units	Casing	Camera	Thick	Thin
		(a)	(b)	2024 -T3	2024 -T3
ρ	kg/m^3	1.18	1.78	2780	2780
G	GPa	2.59		26	26
E	GPa	0.93	70	70	70
ν		0.33	0.3	0.33	0.33
A	MPa	80	100	314	374
B	MPa	75	0	207	164
n		0.05		0.233	0.26
C		0.548		0.0083	0.002
m		2		1.34	1.34
T_M	K	562		750	750
T_R	K	293		293	293
ϵ_o	1/ms	1×10^{-5}		1×10^{-5}	1×10^{-5}
C_p	J/(kg K)	1300		960	960
ϵ_f (c)		0.1	0.1	0.22	0.22

Parameter	Units	Battery
ρ	kg/m^3	1.855
E	MPa	500
ν		0.1
Curve for foam		(0, 6) (0.2, 7) (0.4, 22) (0.5, 48)
Tensile Cutoff ϵ_1 (d)		±0.1

(a) Landing gear used the same material parameters as the casing.
(b) Camera was modeled as an elastic-perfectly-plastic material.
(c) Effective plastic strain for element removal. A strain to failure of 0.22 calibrated against the tensile test was used.
(d) Effective principal strain for element erosion. Data for the thick plate were taken from the Mat-Web website.

3.2. Drone - material model

Drone parts that were polycarbonate (casing, landing gear) were modeled using a plasticity model for simplicity, and following Ali et al. [11] the battery was modeled as a crushable foam. High-speed videos and finite element computations revealed:

1. In the cases wherein the drone does not perforate, the impact starts with the motors, followed by severe deformation of the drone casing and landing gear.
2. In the cases wherein the drone perforates the plate, the process starts with the two front motors. They initiate two holes at their respective impact sites, and the momentum of the drone drives ductile cracks from these holes that coalesce. Upon coalescence, the remaining momentum of the drone leads to petalling as it passes through.

The flow strength of the casing material and camera was described using the Johnson and Cook [12] model as

$$\sigma_{eq} = \left(A + B\,\epsilon_p^n\right)\left(1 + C\,\log\left[\frac{\dot{\epsilon_p}}{\dot{\epsilon}_\circ}\right]\right)\left(1 - \left[\frac{T - T_R}{T_M - T_R}\right]^m\right), \quad (1)$$

where the first term and the terms in the first set of parentheses on the right hand side represent the quasi-static hardening curve, wherein A is the yield strength, B is the hardening coefficient, n the hardening exponent. The terms in the second set of parentheses model a logarithmic dependence of strength due to the strain rate, which is described by the constant C, and ratio of strain rate to a reference rate $\dot{\epsilon}_p/\dot{\epsilon}_\circ$. The reference rate is usually the rate of the quasi-static tensile test. The final set of parentheses describes softening due to temperature increase, and this is assumed to depend on the temperature, T, reference temperature, T_R, and T_M the melting temperature of the aluminum. The latter does not play a role in this work as the impact velocities are not high enough to cause thermal softening.

Johnson-Cook model material parameters are listed in Table 3. We first used the high-strain rate testing data from Fu et al. [13] for modeling the casing. However, these parameters resulted in over prediction of the peak loads; therefore, we take material parameters from Dwivedi et al. [14] following Olivares et al. [4] who validated the model parameters by finite element analysis of drop-weight tests on the casing. Owing to the kinematics of the drone components after the impact of the first motor, strength and failure of the casing is crucial in predicting the loads on the plate. Strain-to-failure for the casing was adjusted through trial-and-error until the simulation results were qualitatively similar to the videos.

The camera was modeled as an elastic-perfectly plastic material and the parameters are also shown in Table 3.

Following Olivares et al. [4], the Lithium ion battery was modeled as a crushable foam (*MAT_CRUSHABLE_FOAM, in LS-DYNA); Li-Ion battery material properties were taken from Ali et al. [11]; parameters are shown in Table 3. A tensile stress cut-off was used to model tensile failure. Eroding surface to surface contacts were also added to the battery to assure that the battery would perforate and erode during the process.

3.3. Target and plate model

The target plate assembly includes a front frame, back frame, flat plate, two I-Beams, two back structures, four spacers and four load cells for the flat plate assembly. Bolts were added to the frame during refinement of the model but were deemed unnecessary as they did not change the force histories and were removed from the model. Nodes comprising the bottom leg sections of the full structure were fixed in all six degrees of freedom (three translational and three rotational). The frame, load cells, I-Beams, full structure and flat plate were also attached with the contact tiebreak to keep the flat plate assembly together. The latter were modeled in SolidWorks, imported into Hypermesh and meshed. See Table 2 for mesh and element detail; and see meshed models in Fig. 7.

McNeill [10] carried out tensile tests on the AA 2024-T3 material used in the tests, and calibrated the hardening part of the Johnson-Cook model. Tensile test simulations, with 2-mm element size, were carried out and the failure strain (0.22) was calibrated. The latter approach mitigates the well-known element size effect when element removal is used to model tearing and penetration of the target.

Thick and thin plates have different strength behavior and properties used in the simulations are tabulated in Table 3. Johnson-Cook rate parameters for the aluminum were taken from Corona and Orient [15].

3.4. Computational details

The completed model is exported as a solver file and run, using a Linux command, with the explicit dynamics time integration solver in LS-DYNA. Simulation runtime and plot output frequency was input to match the sampling frequency of the load cells. Simulations were carried out on 15 Intel Xeon (2.3 GHz) processors with 65 Gigabytes of RAM in each. Typical run times were between 3 hrs to 5 hours.

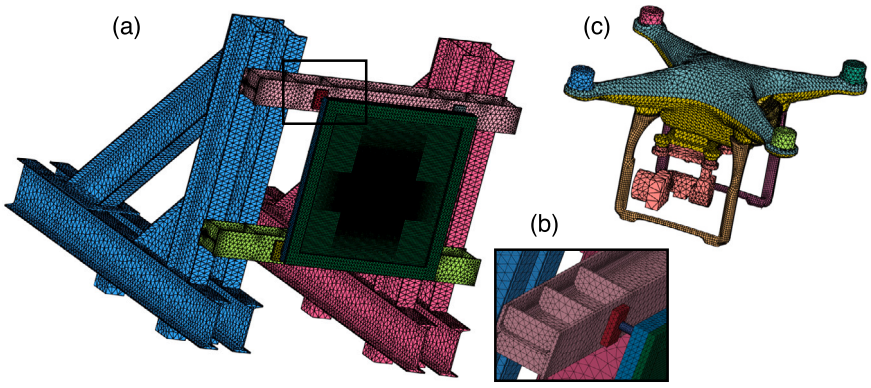

Fig. 7. (a) Structure with frame and target plate; note the denser mesh in the center of the target. (b) Inset shows detail of load cell. (c) Fully assembled drone with mesh.

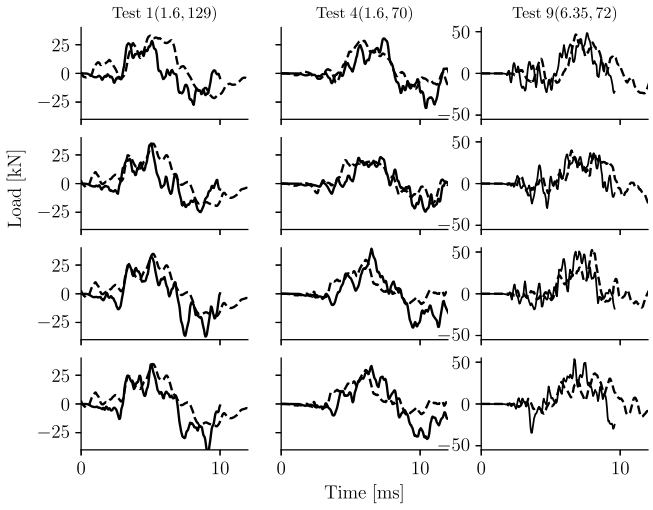

Fig. 8. Load histories compared with simulations results. Simulation results are shown as solid lines. Columns are arrayed as Load cell 1 through 4.

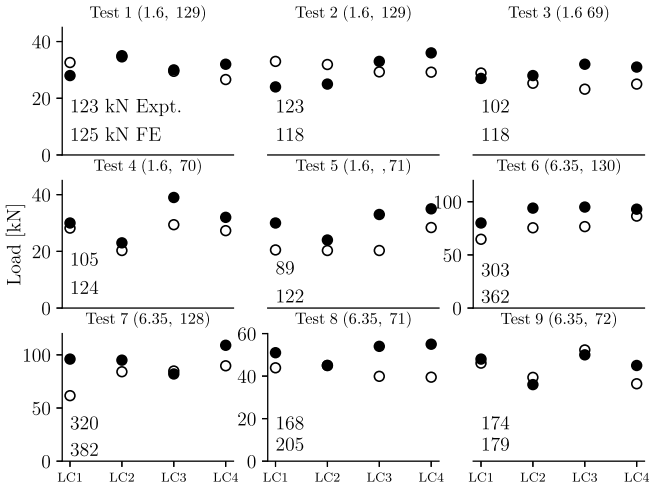

Fig. 9. Comparison of the peak and total loads obtained from experiment (open symbols) and simulation (filled symbols). The sum of the peak loads from the four load cells is also compared - number at the top is experiment and the number at the bottom is from simulation.

4. Finite element results

4.1. Load plots

Load histories from the load cells are compared with the simulation results in Fig. 8.

In Test 1 (1.6, 129), the peak loads and the period of the signal are captured in the simulation. The unloading response, owing to the dynamics of the joint, and approximations in the load cell modeling is not well captured. But this is not too restrictive as the damage to the plate occurs over the period of the first pulse. In Test 4 (1.6, 70), the load corresponding to Load cell 3 is over predicted by 34%. In Test 9 (6.35, 72), the peak load in Load cell 4 is over predicted by as much as 47%.

To assess the potential damage of a drone impact, the peak load is crucial, and a comparison of the experimental peak loads with the simulation results is presented in Fig. 9. Open symbols are peak loads from the experiments and filled symbols are from the simulations. The poorest prediction is for Test 5 (1.6, 71) and the total load (sum of the peak loads from the four load cells) is over predicted by 37%.

In all of the tests, note that there is an initial bump in the experimental curve and this corresponds to the blast pressure of the air from the cannon and this was not modeled in our simulations. Additionally, the behavior of the joint where the plate is attached to the frame and the unloading behavior of the load cells were not modeled.

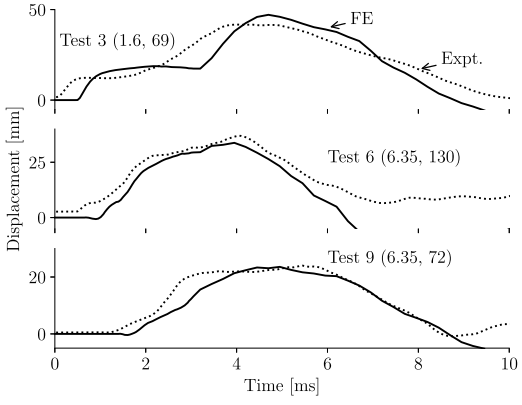

Fig. 10. Comparison of experimental deflections of the center of the plate obtained from Digital Image Correlation with deflections from the finite element simulations.

4.2. Deflection plots

High-speed imaging was used to obtain video of the deforming speckle pattern on the back side of the plate. Digital Image Correlation algorithm (Vic-3D, Correlated Solutions Inc.) was used to analyze the images and calculate the in-plane and out-of-plane displacements. Of interest is the out-of-plane displacement of the plate, which is com-

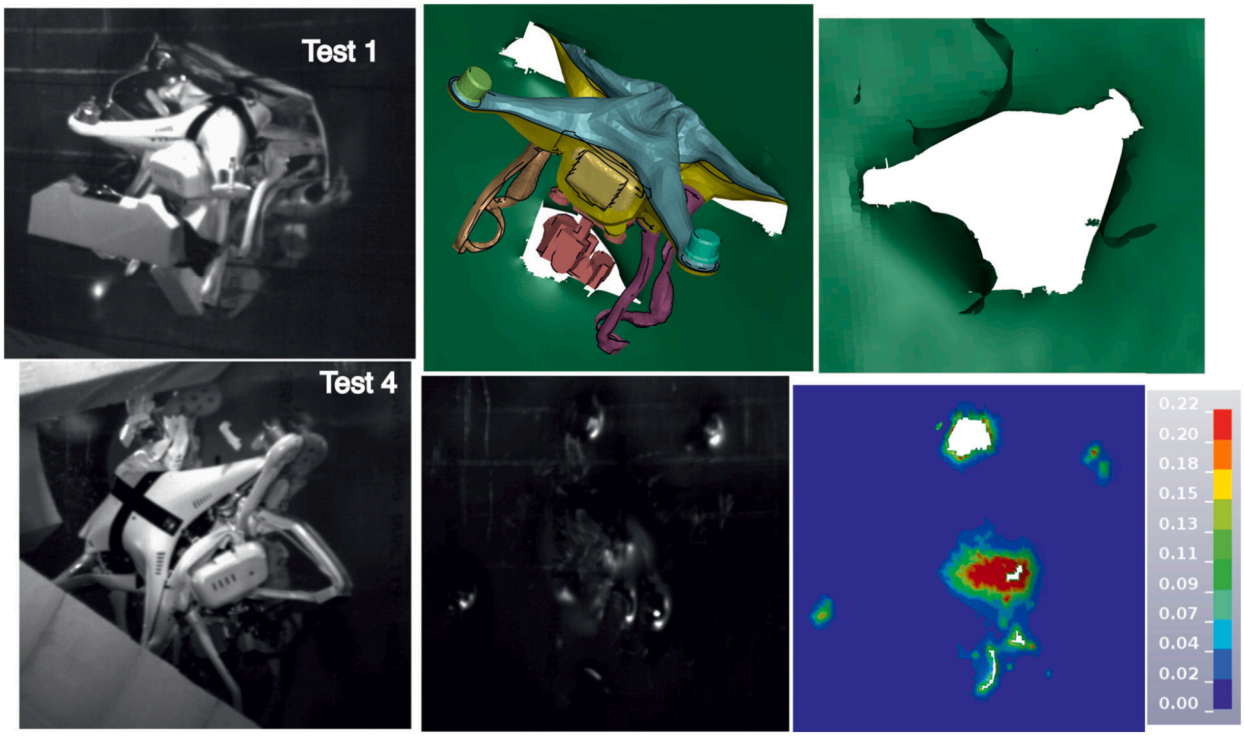

Fig. 11. Top: Test 1 (1.6, 129) photo from high-speed video and simulations results. There was full penetration in the test. Bottom: Test 4 (1.6, 70) photo from high-speed video and simulation results. Dents caused by the motors, battery, camera and drone are seen in the photo extracted from the video. Corresponding plastic strain contours from simulation are also shown.

pared with the deflections predicted by the simulation in Fig. 10; and it can be seen that the agreement is excellent. The shape of the deflection histories is well predicted and the peak deflection differs by less than approximately 15%. Appendix A compares images from the high-speed cameras with images from the finite element simulations.

4.3. Qualitative discussion of results

Fig. 11 presents images from the high-speed video of the test. Corresponding images from the simulations are shown as well. In the case of Test 1 (1.6, 129), there was full penetration of the thin plate. Note that the perimeter of plate that is torn out approximately corresponds to a bounding polygon that can be circumscribed around the drone. Simulations results in Fig. 11 show significant petaling of the plate around the perforated region and is also observed in the post-test photos of the plate.

In Test 4 (6.345 130), the drone impacted and bounced of the plate. Dents caused by the impact, in turn, of the motor, battery, and camera are seen. In the simulation, owing to the element removal scheme, there is a hole where the first motor impacted (but there was no corresponding hole in the experiment). Zones of high plastic strain corresponding to motor, battery, and camera impacts are also seen in the simulation.

It is useful to gather some observations from all of the computational results.

1. The finite element modeling of the experiments indicates that for the orientation of the drone, the sequence of impact is as follows: front motors, camera, casing, battery, and rear motors.
2. For load histories in each of the load cells, the peak loads are predicted to within 25% of the experimental value.
3. For total loads (sum of the peak loads in the four load cells), the finite element results are bounded by 20%, except in Test 5 (1.6, 71) the total experimental load differs from the prediction by 37%. We suggest that in this instance the impact of the landing gear also influences the impact event, and the material model parameters for the landing gear are different from the parameters for the casing.
4. Predictions of the deflection history of the center of the plate are in excellent agreement with the experimental histories.
5. Features of the perforation observed in the plate are qualitatively well reproduced in the simulations.
6. The half-period of 5-6 ms observed in the experimental load histories are well reproduced.

In the next section, we present the modal analysis of the target and show that the source of the period is the natural frequencies of the plate and the structure on which it is mounted.

4.4. Period observed in load histories

The speed of sound in aluminum (≈ 5 km/s), and structural bending wave speed (of the order of 100 m/s) emanating from the impact location to the edges of the plate cannot account for the observed period. To further understand this, a single model comprising the plate and structure was created (see Fig. 12); the latter is required to be able to carry out a linear modal analysis. If the model comprised several parts and contact algorithms, the vibration analysis is rendered non-linear. The model was fixed on the four legs and four blocks (that represent the cross beams in the physical structure) at the bottom of the structure.

Natural frequencies were computed for this structure using LS-DYNA implicit solver. Using Mode Participation Factors and Effective Masses, the natural frequencies that contribute to the dynamics of the structure can be identified. These factors measure the amount of mass moving in each direction for each mode which means that a high value would indicate the mode will be excited by excitation in that direction.

A total of 30 modes were calculated and a few are listed in Table 4. Some of these modes were eliminated using the mode participation factors, and effective masses as they did not excite the structure significantly and were deemed negligible in their effect on the dynamics of the structure. The drone was traveling in the y-direction and there-

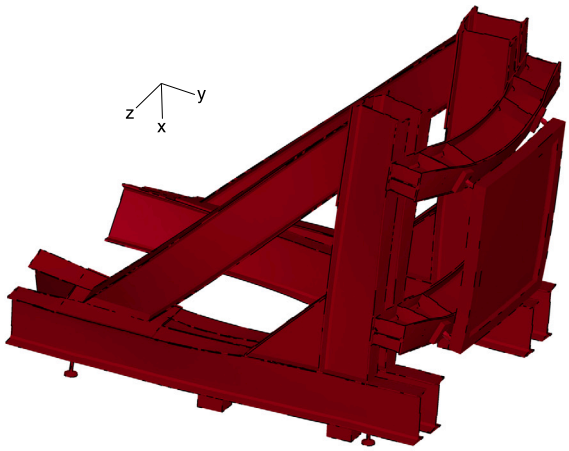

Fig. 12. Modal deformation for mode 6.

Table 4
Mode Participation Factor and Effective Mass.

Mode	Period [ms]	γ y-dirn.	M_{eff} y-dirn.
1	40	-0.034	1.16E-3
6	12.	544.	2.94E5
7	10.	42	1.787E3
8	10.	-141	1.987E4
9	9.	596.11	3.599E5
14	6.82	110	1.211E4
20	5.69	-168.9	2.85E4

γ Mode participation factor.
M_{eff} Effective mass.

fore the participation factors and effective masses for the y direction were considered for choosing the most important modes. Making reference to the table, Mode 1 has a period of 40 ms, but very low effective mass (M_{eff}) and participation factors (γ) compared to the other modes. Mode 6 and 9 had the highest participation factors and effective mass. The latter have periods of 12 and 9 ms, respectively. Modes 7, and 8 with periods of 10 ms are in between. Accordingly, the natural frequencies of the plate-frame structure explain the observed period of 10 ms.

5. Analytical modeling

The previous sections provide an appreciation of the complex workflow (a sequence of 4 softwares), computational power, expertise, and time involved in the development of the finite element model. Consequently, it is useful to assess the possibility of developing simplified models of the impact of drones onto plates. To aid this development, the finite element simulations provide the following insights.

1. In the non-perforation case, the peak load is a consequence of the sequence of impact of the drone components. We checked this by running component impact simulations (not shown here).
2. Maximum central deflection depends on the localized impact of highest-mass components.
3. When the drone impacts the plate, the time interval between component impacts depends on the geometric configuration of the drone and the impact velocity. For example, time interval between first motor impact and second motor impact is well approximated by the distance of the second motor from the plate over the impact velocity.
4. In the perforation case, the process starts with the heaviest component that first impacts the plate. For the orientations of the drone observed in the tests, it is the motors that initiate the perforation process.

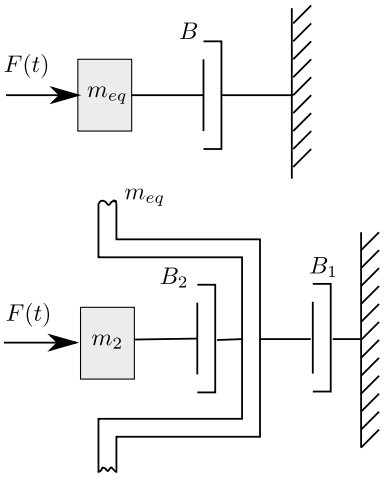

Fig. 13. Top: simplified model for non-perforation case. Blunt object impacts the plate modeled as a mass (m_{eq}) and dashpot (B). Bottom: simplified model for perforation case. Blunt object perforates a plug in the plate of mass m_2 which is connected to the rest of the plate of mass m_{eq} through dash pot B_2. Dashpot, B_1 grounds mass m_{eq}. Figure is adapted from Levy and Goldsmith [17].

An excellent review of simplified impact and perforation models may be found in Corbett et al. [16]. We chose the model developed by Levy and Goldsmith [17] for estimating the peak load, deflection of the plate for both of the perforation and non perforation cases. To estimate the ballistic limit (this is the threshold velocity below which the drone will *not penetrate* the plate), the model from Woodward [18] was adopted.

5.1. Force history - non perforation

Levy and Goldsmith [17] developed expressions to estimate the force of a rigid object impacting a circular metal plate fixed at the circumference. As shown in Fig. 13, the plate is modeled as an equivalent mass (representing the moving part of the circular plate) and a dashpot, and the projectile force is $F(t)$. Taking the dashpot constant as B, mass of the projectile as m_p, and deflection of the center of the plate as w_0, Newton's law yields

$$F(t) = m_{eq}\frac{d^2w_0}{dt^2} + B\frac{dw_0}{dt} = -m_p\frac{d^2w_o}{dt^2}. \tag{2}$$

Solution of this equation is

$$w_0(t) = \frac{m_pV_{op}}{B}\left[1 - exp\left(-\frac{B}{m_p + m_{eq}}t\right)\right], \tag{3}$$

here, elastic effects are ignored and the permanent central deflection $w(\infty) = m_pV_{op}/B$, and V_{op} is the initial velocity of the system at the start of plastic deformation, and $V_{0p} \approx V_0$, the initial velocity. The latter implies that the central equivalent mass of the plate is small compared to the mass of the plate. Levy and Goldsmith [17] follow Calder and Goldsmith [19] and take the deflection of the plate as $w(r) = w_0exp(-ar)$, where a is a constant, r is the radial coordinate of the plate and w_0 is the central deflection parameter. They assume that all the kinetic energy is transformed into plastic deflection of the plate (of thickness h), use plate theory, and show that the central deflection is governed by

$$w_0^2\left[1 + \frac{\alpha a^2}{16\sigma_y}w_0^2\right] = \frac{2(1 - \nu + \nu^2)^{1/2}}{\pi\sigma_y h}m_pV_0^2, \tag{4}$$

which upon noting that $\alpha a^2w_0^2/16\sigma_y << 1$ for aluminum and 0 for mild-steel, w_0 becomes (for $\nu = 0.3$)

$$w(\infty) = V_0\sqrt{\frac{2(1 - \nu + \nu^2)^{1/2}}{\pi\sigma_y h}m_p} = 0.752\sqrt{\frac{m_p}{\sigma_y h}}. \tag{5}$$

In the limit of Eq. (2) and Eq. (5) yields an expression for B as

$$B = 1.33\sqrt{m_p \sigma_y h}\frac{V_{0p}}{V_0} = 1.33\sqrt{m_p \sigma_y h}. \tag{6}$$

We now turn to a value for m_{eq}. Taking the deflected shape as $w(r) = w_0 exp(-ar)$, we can write the kinetic energy as

$$E_k = \frac{1}{2}\int_0^R \left(\frac{dw}{dt}\right)^2 dm = \pi\rho h \left(\frac{dw_0}{dt}\right)^2 \frac{1}{4a^2}. \tag{7}$$

Which is the total kinetic energy of the plate and must be equal to the kinetic energy of the equivalent mass m_{eq} which yields

$$\frac{\pi\rho h}{4a^2}\left(\frac{dw_0}{dt}\right)^2 = \frac{1}{2}m_{eq}\left(\frac{dw_0}{dt}\right)^2, \tag{8}$$

which in turn gives an expression for the equivalent mass as

$$m_{eq} = \frac{\pi\rho h}{2a^2}. \tag{9}$$

Substituting for m_{eq} and B in Eq. (3), the above development yields an expression for the plastic deflection of the center of the impacted plate

$$w_0(t) = 0.752 V_0 \sqrt{\frac{m_p}{\sigma_y h}} \tag{10}$$

$$\left[1 - exp\left(-\left\{\frac{1.33\sqrt{m_p \sigma_y h}}{m_p + m_{eq}}\right\} t\right)\right]. \tag{11}$$

This expression then yields the force on the plate as

$$F(t) = -m_p \frac{d^2 w_0}{dt^2}, \tag{12}$$

$$= \frac{1.33 m_p^{5/2}\sqrt{\sigma_y h}}{(m_p + m_{eq})^2} v_0 e^{-\left(\frac{1.33\sqrt{m_p\sigma_y h}}{m_p + m_{eq}}\right)t}, \tag{13}$$

and maximum force is

$$F_{max} = \frac{1.33 m_p^{3/2}(\sigma_y h)^{1/2}}{(m_p + m_{eq})^2} M_0, \tag{14}$$

where $M_0 = m_p V_0$.

Equations (10) and (12) yield expressions for central deflection of the plate and total force histories, respectively. There are two ways in which the force-history can be used. First, the total mass of the drone can be used for m_p. Second, m_p can be taken to be the mass of the components that impact the plate in the order: motor, camera, casing, and rear motors. In the latter case, with a knowledge of the geometry of the drone, and assuming no change in impact velocity, we can estimate the time interval between impact of the most significant components. Accordingly, we can compute the load history corresponding to each of the significant components, time shift the histories based on the computed intervals, and then sum the histories.

The latter process implies that we are invoking superposition, which is not valid when the structure deforms plastically. However, the external boundary of the plate is elastic (as observed in the simulations) and the plasticity is localized to the central region of the plate. Therefore, to obtain force histories in the elastic portion of the plate, there is no bar in summing the force histories.

A further choice can be made with regards to strength - we can use the yield (σ_y) or ultimate strength (σ_u) value and obtain lower and upper bounds for the force histories.

Parameters used in the analytical model are presented in Table 5. Time intervals between impacts of the various components were estimated by dividing distances by the impact velocity. Results for Test 5 are shown in Fig. 14. Parameter a governs the shape of the deflected plate; Levy and Goldsmith [17] use 1/25 mm^{-1}.

Table 5
Parameters for analytical model - non-perforation.

	Units	Value	Source
B	N-ms/mm	692	
a	1/mm	1/25	Levy and Goldsmith [17]
σ_y	MPa	314	McNeill [10]
σ_u	MPa	456	McNeill [10]
μ	Nms/mm^2		
Drone	gm	1160	Dadouche et al. [9]
Motor	gm	53.8	
Camera	gm	181	
Casing	gm	233.2	
Battery	gm	371.2	
Camera	ms	$71/Vo$	Time interval
Body	ms	$85/Vo$	for impacts (a)
Battery	ms	$91/Vo$	
Back Motors	ms	$250/Vo$	
Plate Diameter	ms	1041	
Plate Density	g/mm^3	2.7e-2	

(a) Based on the drone configuration, we can estimate the time interval between impacts of the various components. Here, Vo is the impact velocity.

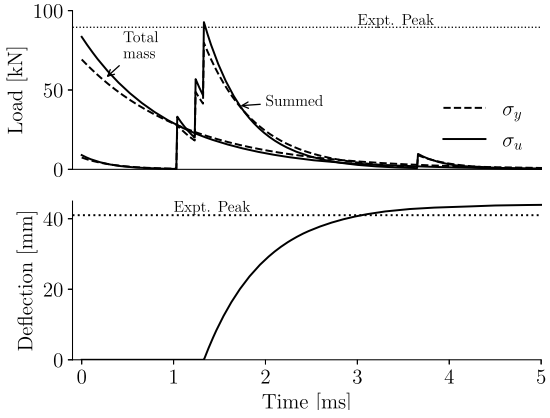

Fig. 14. Levy-Goldsmith model results for Test 5. Top: load history, and bottom deflection of center of plate. Dotted lines are experimental peak values.

Note that peak loads computed with the total mass of the drone and either σ_y and σ_u are below the peak experimental load. In contrast, histories computed by summing the effects of the sequential impact of the significant masses bracket the experimental peak force. The deflection peak predicted for Test 5 is in excellent agreement with the experimental peak. In Table 6 predictions for Test 3 through Test 9 are compared with experimental loads, and overall the model is able to predict the peak force to within 13%.

It bears emphasis that this deflection-history plot is made with only the mass of the battery in Eq. (10); the histories are not summed as in the force plot. The rationale behind this is as follows. As discussed, the loads are measured at the four corners of the plate; that are far away from the point of impact where the response of the plate is elastic. In contrast, the deflection is measured at the center of the plate. From the finite element simulations, the motor impacts the plate first, away from the center, then the camera, and finally the battery. This leads to the most significant deflection and plasticity at the center of the plate. If we sum the deflection histories, as we did the load versus time traces, the central deflection would be significantly higher than in the experiment. More importantly, on account of the significant plasticity at the center of the plate, *superposition is not valid.* Yield was used in the computation of the deflection history as it obtains an upper bound.

5.2. Force history - perforation

The lumped-parameter model developed by Levy and Goldsmith [17] is shown in Fig. 13. In the perforation process, a plug is sheared out from the plate. The plug mass is m_2 and its dashpot is B_2, the mass of the non perforated plate is $m^*_{eq} = m_{eq} - m_2$ and its dashpot is B_1, which is connected to a rigid base. Displacements of the masses are w_1 and w_2. The equations of motion are

$$m_2\frac{d^2w_2}{dt^2} + B_2\left(\frac{dw_2}{dt} - \frac{dw_1}{dt}\right) = F(t) = -m_p\frac{d^2w_2}{dt^2}$$
$$B_2\left(\frac{dw_2}{dt} - \frac{dw1}{dt}\right) = m_{eq}\frac{d^2w_1}{dt} + B_1\frac{dw_1}{dt}. \quad (15)$$

Solving these equations for w_1 and w_2 and taking $v_2 = dw_2/dt$, Levy and Goldsmith [17] obtained

$$H\dot{v}_1 + C\dot{v}_1 + Dv_1 = 0, \quad (16)$$

where $H = m^*_{eq}\frac{m_2+m_p}{B_2}$, $C = \left(m_2 + m_p\right)\left(1 + \frac{B_1}{B_2}\right) + m^*_{eq}$, and $D = B_1$. The above equation has the solution $v_1 = b_1 exp(\lambda_1 t) + b_2 exp(\lambda_2 t)$, where

$$\lambda_{1,2} = \frac{1}{2H}\left(-C \pm \sqrt{C^2 - 4HD}\right), \quad (17)$$

which can be substituted for $v_2(t)$, and then v_2 is substituted in Eq. (15), which in turn is solved for $v_1(t)$ Levy and Goldsmith [17] further assume that perfectly plastic loading of the plate and plug demands

$$m_pV_o = (m_2 + m_p)V^*_{20} + m^*_{eq}V^*_{10}, \quad (18)$$

where V^*_{10} is the value of the equivalent plate mass velocity at the plug periphery acquire after the impact of the projectile. Term V^*_{20} is the common velocity of the plug and projectile after impact. Taking these two velocities as equal yields

$$\left(m^*_{eq}\lambda_1 + B_1\right)(b_1/B_2) = -\left(m^*_{eq}\lambda_2 + B_1\right)(b_2/B_2). \quad (19)$$

Combining Eq. (19) and Eq. (18) yields

$$b_1 = \left[\frac{m_pV_0}{m_p + m^*_{eq} + m_2}\right]\left[\frac{m^*_{eq}\lambda_1 + B_1}{m^*_{eq}\left[\lambda_2 - \lambda_1\right]}\right], \quad (20)$$

and

$$b_2 = \left[\frac{m_pV_0}{m_p + m^*_{eq} + m_2}\right] - b_1. \quad (21)$$

The force on the projectile is

$$F_2(t) = -m_pV^*_2 = -m_p\left(m^*_{eq}\left(\frac{-D}{C}\right) + B_1 + B_2\right)\left(\frac{-b_2D}{CB_2}\right)e^{-\left(\frac{D}{C}\right)t} \quad (22)$$

The term B_1 is identical to the B term for the non-perforation case. Viscous damping coefficient is estimated using the method of Awerbuch and Bodner [20] to obtain

$$B_2 = 2\pi r_e h\left(\frac{\mu}{e}\right), \quad (23)$$

where r_e is the effective radius of the plug, μ the viscous coefficient for shearing deformation, and e is the radial width of the shear zone.

In the non-perforation model, the forces of the separate components of the drone are calculated and added together. In the present case, the penetration model assumes that the force will be produced by the impact of a single mass, as once a component of the drone has penetrated it will not apply any further force to the plate. Through iterative tests and comparison to the experimental results, it is shown that the battery is the component creating the peak force in the penetration cases. The motors of the drone are the component to first penetrate, but will not lead to the largest impact force. Analogous to the battery being the main factor in the deflection of the plate, it also leads to the largest impact force with penetration.

Table 6
Force and Deflection predictions using Levy-Goldsmith model.

	F_{max} (a) [N]	F_{max} (b) [N]	Expt. [N]	w_{max} [mm]	Expt. [mm]
1	128	157	123	-	-
2	128	157	123	-	-
3	79	92	102	44	40
4	81	96	105	45	41
5	82	96	89.5	46	39
6	268	312	303	42	37
7	268	312	320	41	41
8	130	1540	168	23	22
9	134	154	174	23	24

(a) Computed with σ_y.
(b) Computed with σ_u.

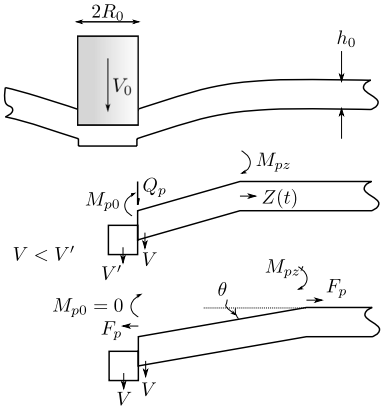

Fig. 15. Top: blunt object impacting an infinite plate. Middle: Stage 1 - Plug shearing. Bottom: Stage 2 - membrane stretching. Figure is adapted from Woodward [18].

To verify the validity of the first analytical model, the results of all experiments are compared in Table 6. It bears emphasis that:

1. Non-penetration load - computed by summing component histories.
2. Non-penetration deflection - computed using only the battery because it impacts the center.
3. Penetration load - computed using only the battery as the motor impact, which leads the penetration, does not result in significant loads at the corners.

6. Penetration velocity

The second analytical model developed is based on the perforation model developed by Woodward [18]. He proposed that "The ability of a projectile to perforate a target can be assessed by comparing its kinetic energy with the mechanical work required to produce a hole of the appropriate size and shape in the target, Woodward [18]." He further assumed that the impact of a thin plate by a blunt projectile can be characterized as an infinite beam problem. Upon impact, shear sliding deformation is created in the plate and the material bends around a plastic hinge. The reaction to the impact is then split into two stages shown in Fig. 15, with formulas characterizing each.

6.1. Stage 1

In Stage 1 of the impact, the projectile is shearing the plate and creating a plug from it. The velocity of this plug in Stage 1 will be higher

than the velocity of the plate surrounding it. This stage then ends with either the plug completely shearing from the plate or it moves on into Stage 2. Impulse of the shear force $2Q_P$ to the change in momentum on either side of the plug-plate interface gives

$$GV_0 - GV' - \frac{m_0 R_0^2}{2}V' = \int 2Q_p dt == \frac{m_0 z}{2}(R_0 + \frac{1}{3}z)V \tag{24}$$

where $m_0 = 2\pi\rho h_0$;
G is projectile mass;
V_o is the projectile impact velocity;
V is the velocity of the plate adjacent to the plug;
h_0 is the plate initial thickness;
R_0 is the projectile radius;
z is the hinge position, measured from the plug-target interface;
ρ is the plate density;
t is time.

Change in angular momentum to the impulse of the torque provides

$$-GV_0 z + GV'z + \frac{1}{2}m_0 R_0^2 V' z + \frac{1}{3}m_0 z^2 V(R_0 + \frac{1}{4}z), \tag{25}$$

$$= -2\int (M_{p0} + M_{pz})dt \tag{26}$$

where the plastic hinges have moments M_{po} and M_{pz} at the plug-target interface R_0 and at the periphery of the dished region $R_0 + z$. Taking the material to be rigid-plastic with yield strength σ_y, and the reduced section contact area at the plug-target interface to have a thickness of h_0 gives

$$Q_p = \frac{\pi}{\sqrt{3}}R_0 h\sigma_y, \tag{27}$$

$$M_{p0} = \frac{\pi}{4}R_0 h^2\sigma_y, \tag{28}$$

and

$$M_{pz} = \frac{\pi}{4}(R_0 + z)h_0^2\sigma_y. \tag{29}$$

All of the above equations can be converted to obtain a quadratic equation for z, which can be solved at each time step. From the initial position of the hinge z is assumed to be $R_0/3$ and the value increases with time as the hinge moves towards the circumference. Velocity V of the plate increases with time till it equals the plug velocity V' at which time sliding ceases h becomes zero and a plug is formed and failure has occurred.

At this time, shearing of the plug has stopped, the relative plug-plate velocity is zero, and the plate continues to stretch as a membrane with bending at hinge located at z.

6.2. Stage 2

In Stage 2 of the impact, the projectile has stopped shearing the plate, so the plug and plate are still connected and moving at the same velocity, eventually stopping. In this stage the stretching of the aluminum plate must be added to the calculations for transfer of energy. The stretching of the aluminum plate is assumed to act as a tapered tensile sample with rigid linear work hardening, σ_y and is shown in Fig. 3 in the article by Woodward [18]. The membrane force is then

$$F_p = \pi R_0 h\sigma_y \tag{30}$$

and the bending moment at the plug-target interface is zero. Using the results of Grzebieta and Murray [21], which accounts for the membrane loads, the reduced moment M'_{pz} is given in terms of M_{pz} as

$$M'_{pz} = M_{pz}\left(1 - \left[\frac{R_0 h}{(R_0 + z)h_0}\right]^2\right). \tag{31}$$

Table 7
Parameters used in penetration model.

Variable	Units	Value
Plate Thickness	mm	1.6
Projectile Diameter	mm	31
Projectile Mass	gm	52
Density	kg/m^3	2780
Target Yield (σ_y)	MPa	314
β	MPa	189.
span	m	0.960
Failure Strain		0.3
Young's Modulus	GPa	70

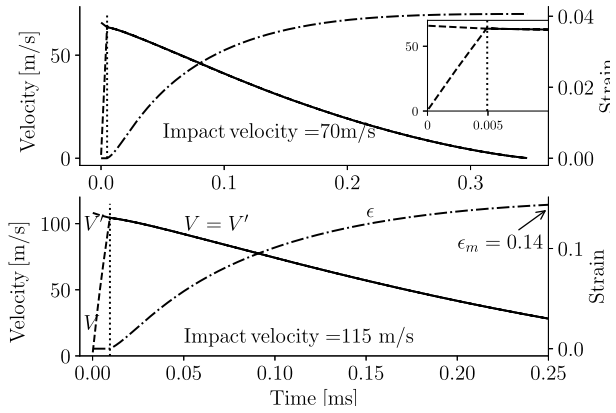

Fig. 16. Velocity and strain histories of the plug and projectile obtained using Woodward's analysis. Left axis is velocity and right axis is membrane strain. Dotted vertical line separates Stage 1 and Stage 2. Top: impact velocity of 70 m/s. Inset shows detail of graphs in Stage 1. Bottom: plots for impact velocity of 115 m/s.

Angular momentum provides

$$\frac{1}{2}Gz\Delta V cos\theta + \frac{1}{2}m_0 R_0^2 z(R_0 + \frac{1}{3}z)\Delta V + \tag{32}$$

$$m_0(R_0 + \frac{2}{3}z)V\Delta z = 0, \tag{33}$$

where θ is the angle through which the plate is bent, Δt is the time step, ΔV is the change in velocity and Δz the change in the hinge position.

A failure criterion for the plate was derived by computing the stretch of the tapered specimen. Flow behavior is taken to be linear as $\sigma = \sigma_y + \beta\varepsilon$, where σ is the flow stress, ϵ the strain and α and β are the hardening constants. Mean strain at failure ϵ_m is given by

$$\varepsilon_m = \left[\frac{\sigma_y\left(\sigma_y \dot{+} \beta\varepsilon_0\right)}{\beta^2\varepsilon_0} ln\left(\frac{\sigma_y + \beta\varepsilon_0}{\sigma_y}\right) - \frac{\sigma_y}{\beta}\right], \tag{34}$$

where ϵ_0 the failure strain from a tensile test. This is the equation for the mean membrane strain in the dished material at fractures.

Change in $\Delta\theta$ over each time increment is converted to an increase in length in the dishing region, which in turn converts to an increment of mean strain $\Delta\epsilon_m$. After each step, the total mean strain is compared with the failure strain from Eq. (34). When failure occurs, the plate is perforated owing to failure at the periphery of the plug.

As the penetration process leads with the motor, we use the motor mass and diameter for the analysis. Using the thin-plate parameters listed in Table 7, the analysis was carried out and histories of the velocity of the plug, projectile and the membrane strain are plotted in Fig. 16. For an impact velocity of 70 m/s, the velocity of the projectile decreases, and the velocity of the plug increases as can be seen in the inset of the graphs at the top. In Stage 2, the plug and the plate decelerate to a stop while the membrane strain does not exceed 0.04; that is, the membrane does not fail, indicating no penetration.

For an impact velocity of 115 m/s, in Stage 2, the velocity of the plug and plate decreases, but the membrane strain reaches the failure strain of 0.14, which was computed using Eq. (34), and thereby indicating penetration of the plate. So, we have established the threshold velocity of penetration to be 115 m/s, which is in good agreement with the experimental observations. Furthermore, for a plate thickness of 6.35 mm plate, impact velocity $>$ 250 m/s was required for penetration; again, this is in accord with the experimental results that no penetration was observed in any of the thick-plate tests for impact velocities below 130 m/s.

7. Summary and conclusion

In this work, we have described work flows to develop a finite element model of a quadcopter which can be used to model impact of quadcopter onto a flat plate. Using impact experiments, we validated the model. The key demonstration in the finite element modeling effort is the use of material models from the literature for the plate and drone components; except for the casing strength properties. The latter point deserves emphasis because we relied on the Johnson-Cook parameters from Dwivedi et al. [14] that were validated through component-level drop tower testing by Olivares et al. [4]. It bears emphasis that when we used polycarbonate data from Fu et al. [13], the peak loads were significantly higher than compared to the experimental values. That is, the deformation response of the casing is crucial for modeling the loads on the plate, as it controls the sequence of impacts onto the plate. In summary, we have answered the stated question of being able to model the impact of a drone assembly without carrying out extensive component-level testing.

A failure strain of 10% is sufficient for all of the drone components; for the plate, data from high-strain rate coupon testing serves the purpose. The peak load, deflection, and period of the pulse the impact induces in the plate are modeled, and accounted for. Experimental peak loads and maximum central deflection of the plate are predicted by the finite element computations to within 20% and 10%, respectively.

More importantly, the validated models provide the insight that allows us to develop the Levy-Goldsmith models at the level of ordinary differential equations of the impact process. The latter obtain predictions of the peak load, and deflection to within 10% of the experimental values. Finally, we used Woodward's model to estimate the threshold velocity for penetration.

There is some room for improvements to the finite element model. Improve the modeling of the boundary condition where the plate is bolted onto the frame. Improve the material modeling for the landing gear. Here, component-level testing and/or material coupon testing has potential to prove useful.

CRediT authorship contribution statement

Jay McNeill: Writing – original draft, Investigation, Formal analysis. **Randall VanDyk:** Writing – review & editing, Writing – original draft, Investigation, Formal analysis. **C.H.M. Simha:** Writing – review & editing, Supervision, Formal analysis, Conceptualization. **Azzedine Dadouche:** Writing – review & editing, Project administration, Investigation, Conceptualization. **David Backman:** Writing – review & editing, Investigation, Data curation, Conceptualization. **Manouchehr Nejad Ensan:** Writing – review & editing, Supervision, Conceptualization. **Javad Gholipour:** Writing – review & editing, Supervision, Investigation, Conceptualization.

Declaration of competing interest

The authors declare no conflict of interest.

Acknowledgements

Technical support from Transport Canada (TC) and Defence Research and Development Canada (DRDC) is gratefully acknowledged.

Appendix A

Images taken from the high-speed video (20,000 frames per second), from Test 1 (1.6, 130) are presented in Fig. A.17. Corresponding images from the simulations are shown for comparison. Below, we list similarities between experiment and simulation, in the observed kinematics and deformation.

1. 0.2 ms: The left motor has impacted; the white arrow indicates the foam block that was part of the sabot used for launching the drone.
2. 0.45 ms: The left motor has started perforating the plate, and the right motor has impacted the plate.
3. 0.7 ms: Both motors have penetrated the plate, and the landing gear has impacted.
4. 0.85 ms: The top cover of the drone has perforated the plate, and the perforations created by the two motors are coalescing, leading to a tear. Significant deformation of the landing gear is visible.
5. 1.45 ms: Almost half of the drone has perforated the plate.
6. 5.7 ms: The entire drone has passed through the plate. A petal in the perforation is visible in both the experiment and the simulation.

Images taken from the high-speed video (20,000 frames per second), from Test 3 (1.6, 70) are presented in Fig. A.18. Corresponding images from the simulations are shown for comparison. Below, we list similarities between experiment and simulation, in the observed kinematics and deformation.

1. 0.95 ms: One of the motors has impacted the plate, and there is some bending deformation in the casing carrying that motor.
2. 1.2 ms: The motor has created a perforation, and there is further deformation in the form of severe bending of the casing.
3. 4.2 ms: The casing carrying the impacted motor has deformed, and the two other motors simultaneously impact the plate denting it. White arrow indicates part of the foam sabot used in launching the drone. Both of the landing gear structures have impacted the plate with significant deformation.
4. 11.45 ms: All parts of the drone have impacted the plate, causing significant deformation and failure, and the drone parts have bounce off. In this image and in the simulation the drone parts are traveling away from the plate. In both the experiment and the simulation, the drone does not perforate the plate.
5. 1.5 ms: In the experiment, a central tear caused by impact of the motor and the battery is seen, additionally dents caused by impacts of the motors and the landing gear are seen. In the simulation, the size of the central perforation is under predicted, and the dents are captured in the simulation.

Data availability

Data will be made available on request.

References

[1] A. Radi, Potential damage assessment of a mid-air collision with a small UAV, Technical Report, Civil Aviation Safety Authority, Monash University, 2013.
[2] Small Remotely, Piloted Aircraft Systems (drones) - Mid Air Collision Sudy, Technical Report, The Department for Transport, UK, 2016.
[3] G. Olivares, T. Lacy, L. Gomez, J. de los Monteros, R. Baldridge, C. Zinzuwadia, T. Aldag, K. Kota, T. Ricks, N. Jayakody, UAS airborne collision severity evaluation, Technical Report, U.S. Department of Transportation Federal Aviation Administration, National Institute for Aviation Research, 2017.

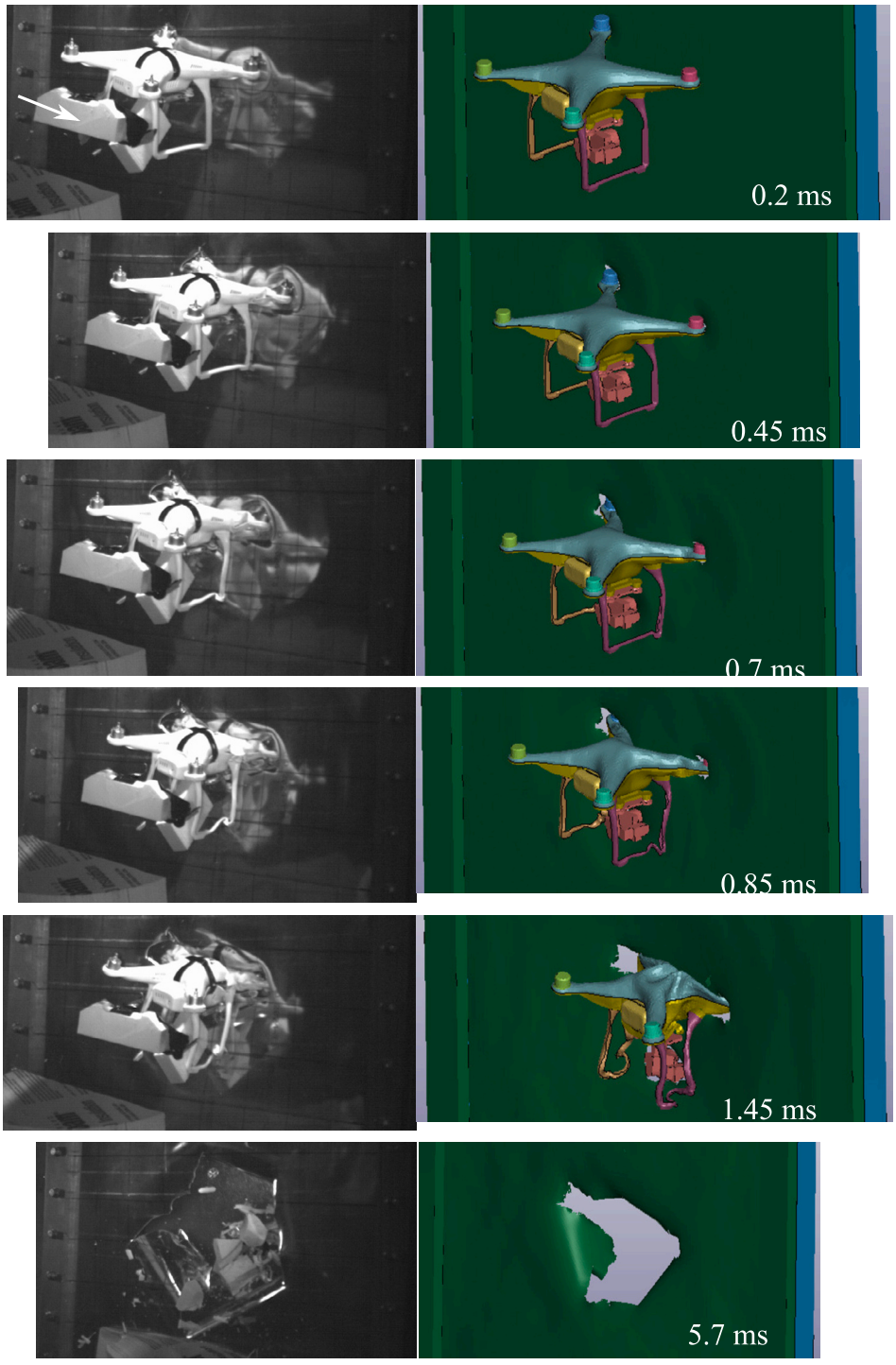

Fig. A.17. Images from high-speed video of Test 1 (1.6, 130).

[4] G. Olivares, L. Gomez, J.E.d.l. Monteros, R.J. Baldridge, C. Zinzuwadia, T. Aldag, Volume II - UAS Airborne Collision Severity Evaluation - Quadcopter, Technical Report, National Institute for Aviation Rsearch, Wichita State University, 2017.

[5] X. Lu, X. Liu, Y. Zhang, Y. Li, H. Zuo, Simulation of airborne collision between a drone and an aircraft nose, Aerosp. Sci. Technol. 118 (2021) 107078.

[6] X. Lu, X. Liu, Y. Li, Y. Zhang, H. Zuo, Simulations of airborne collisions between drones and an aircraft windshield, Aerosp. Sci. Technol. 98 (2020) 105713.

[7] X. Meng, Y. Sun, J. Yu, Z. Tang, J. Liu, T. Suo, Y. Li, Dynamic response of the horizontal stabilizer during UAS airborne collision, Int. J. Impact Eng. 126 (2019) 50–61.

[8] A. Dadouche, D. Backman, C. Vidal, R. Gould, Drone Impact Assessment on Flat Plates: Experimental Results, Technical Report, 2020.

[9] A. Dadouche, B. Galeote, T. Breithaupt, A. Greer, D. Backman, G.L. Li, C. Vidal, R. Gould, Drone impact assessment on aircraft structure: flat plate testing and analysis, Technical Report, National Research Council of Canada, Aerospace Research Centre, 2020, Artwork size: vol. 1 of 2, 34 p.

[10] J. McNeill, Interior, Exterior and Terminal Ballistics of Cannon-Launched Drones, Master's thesis, University of Guelph, 2023.

[11] M.Y. Ali, W.-J. Lai, J. Pan, Computational models for simulation of a lithium-ion battery module specimen under punch indentation, J. Power Sources 273 (2015) 448–459.

[12] G. Johnson, W. Cook, A constitutive model and data for metals subjected to large strains, high strain rates and high temperatures, in: Proc. 7th Int. Symposium on Ballistic, 1983.

[13] S. Fu, Y. Wang, Y. Wang, Tension testing of polycarbonate at high strain rates, Polym. Test. 28 (2009) 724–729, https://doi.org/10.1016/j.polymertesting.2009.06.002.

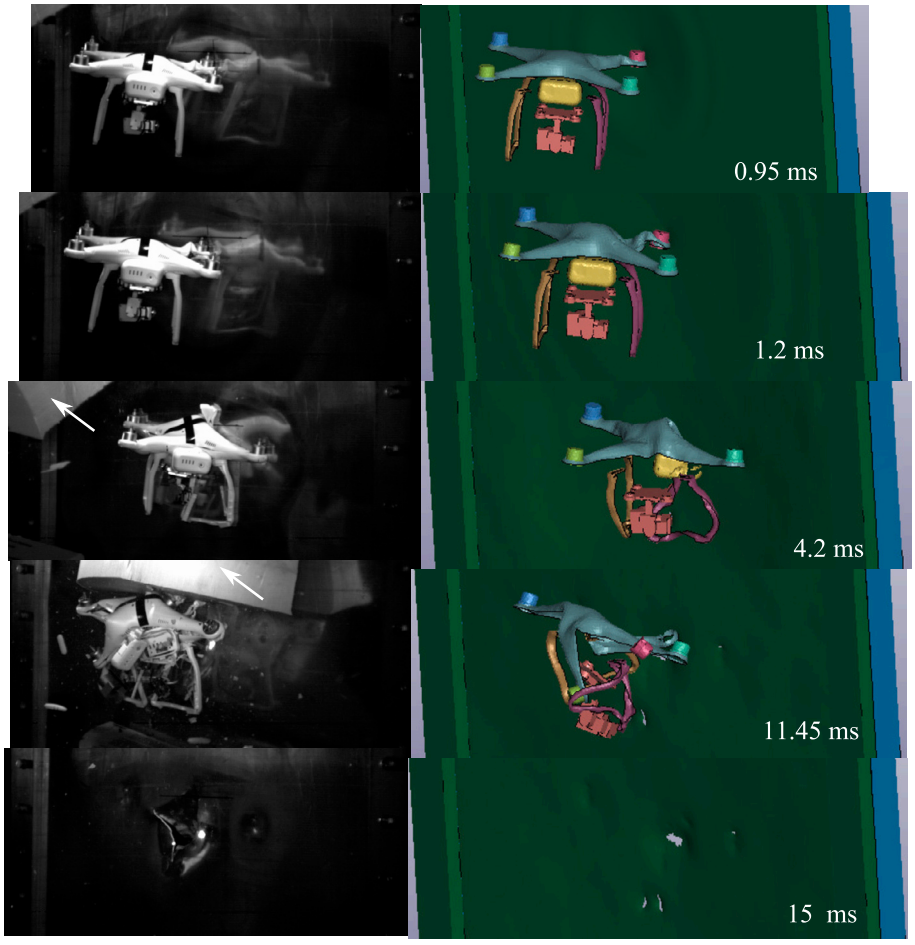

Fig. A.18. Images from high-speed video of Test 3 (1.6, 70).

[14] A. Dwivedi, J. Bradley, D. Casem, Mechanical Response of Polycarbonate with Strength Model Fits, Technical Report ARL-TR-5899, Army Research Laboratory, 2012.
[15] E. Corona, G. Orient, An evaluation of the Johnson-Cook model to simulate puncture of 7075 aluminum plates, Technical Report SAND2014-1550, 1204105, 505013, 2014.
[16] G. Corbett, S. Reid, W. Johnson, Impact loading of plates and shells by free-flying projectiles: a review, Int. J. Impact Eng. 18 (1996) 141–230.
[17] N. Levy, W. Goldsmith, Normal impact and perforation of thin plates by hemispherically-tipped projectiles-I. Analytical considerations, Int. J. Impact Eng. 2 (1984) 209–229.
[18] R.L. Woodward, A structural model for thin plate perforation by normal impact of blunt projectiles, Int. J. Impact Eng. 6 (1987) 129–140.
[19] C. Calder, W. Goldsmith, Plastic deformation and perforation of thin plates resulting from projectile impact, Int. J. Solids Struct. 7 (1971) 863–881.
[20] J. Awerbuch, S. Bodner, Analysis of the mechanics of perforation of projectiles in metallic plates, Int. J. Solids Struct. 10 (1974) 671–684.
[21] R. Grzebieta, N. Murray, The static behaviour of struts with initial kinks at their centre point, Int. J. Impact Eng. 3 (1985) 155–165.